

Adaptive feature capture method for solving partial differential equations with low regularity solutions

Yangtao Deng^a, Qiaolin He^a, Xiaoping Wang^{b,c,*}

^a*School of Mathematics, Sichuan University, Chengdu, 610065, China*

^b*School of Science and Engineering, The Chinese University of Hong Kong, Shenzhen, Guangdong, 518172, China*

^c*Shenzhen International Center for Industrial and Applied Mathematics, Shenzhen Research Institute of Big Data, Guangdong, 518172, China*

Abstract

Partial differential equations (PDEs) with low-regularity solutions pose significant challenges for traditional numerical methods, particularly in complex geometries where mesh generation and adaptive refinement become computationally expensive. While deep-learning-based approaches, such as Physics-Informed Neural Networks (PINNs) and the Random Feature Method (RFM), offer mesh-free alternatives, they often lack adaptive resolution in critical regions, limiting their accuracy for solutions with steep gradients or singularities. In this work, we propose the Adaptive Feature Capture Method (AFCM), a novel machine learning framework that adaptively redistributes neurons and collocation points in high-gradient regions to enhance local expressive power. Inspired by adaptive moving mesh techniques, AFCM employs the gradient norm of an approximate solution as a monitor function to guide the reinitialization of feature function parameters. This ensures that partition hyperplanes and collocation points cluster where they are most needed, achieving higher resolution without increasing computational overhead. The AFCM extends the capabilities of RFM to handle PDEs with near-singular solutions while preserving its mesh-free efficiency. Numerical experiments demonstrate the method's effectiveness in accurately resolving low-regularity problems, even in complex geometries. By bridging the gap

*Corresponding author

Email addresses: ytdeng1998@foxmail.com (Yangtao Deng),
qlhejenny@scu.edu.cn (Qiaolin He), wangxiaoping@cuhk.edu.cn (Xiaoping Wang)

between adaptive mesh refinement and randomized neural networks, AFCM offers a robust and scalable approach for solving challenging PDEs in scientific and engineering applications.

Keywords:

partial differential equations, low regularity, adaptive feature capture method, random feature method

1. Introduction

Partial differential equations (PDEs) are widely applied in diverse fields such as physics, engineering, economics, and biology [1, 2, 3]. Traditional numerical methods, including finite difference [4], finite volume [5], and finite element methods [6], have made significant theoretical and practical contributions to solving PDEs. However, these methods face notable challenges. For instance, complex geometries often lead to distorted mesh elements, which degrade computational accuracy and efficiency [4, 7, 8, 9].

In contrast, the success of deep learning in computer vision and natural language processing [10] has spurred interest in its application to scientific computing. Neural networks, with their universal approximation capabilities [11], have been explored for solving ordinary and partial differential equations (ODEs and PDEs) [12, 13, 14, 15, 16, 17, 18, 19]. Various deep-learning-based approaches have emerged, such as the Deep Ritz Method (DRM) [14], Deep Galerkin Method (DGM) [15], Physics-Informed Neural Networks (PINNs) [17], and Weak Adversarial Networks (WAN) [16]. These methods offer mesh-free alternatives, circumventing the need for computationally intensive mesh generation. However, a critical limitation of these approaches is the lack of reliable error estimation. Without knowledge of the exact solution, numerical approximations often fail to exhibit clear convergence trends, even as network parameters increase [20], raising concerns about their reliability in scientific and engineering applications.

Recent studies highlight the potential of randomized neural networks, such as the Extreme Learning Machine (ELM) [21] or Random Feature Method (RFM) [22, 23], for solving ODEs and PDEs. ELM, a single-hidden-layer feedforward network, randomly initializes hidden-layer weights and biases while analytically optimizing output-layer weights via least squares [24]. This architecture eliminates the need for iterative training of hidden-layer parameters, offering significant computational efficiency over conventional

deep networks. As a mesh-free universal approximator [21, 25, 26, 27], ELM excels in handling PDEs in complex geometries. Extensions like the Physics-Informed ELM (PIELM) [28] have further demonstrated its utility in solving differential equations [25, 26, 29, 30, 28, 31, 32, 33, 34, 35, 36].

Building on these advances, the Random Feature Method (RFM) [25] combines partition of unity (PoU) with random feature functions to solve linear PDEs in complex geometries, achieving high accuracy in both space and time. However, for PDEs with low-regularity solutions, RFM may struggle due to insufficient local expressive power in high-gradient regions. In classic adaptive numerical methods, the mesh as well as the domain may be refined or decomposed, in order to improve the accuracy. Adaptive mesh refinement techniques, such as the moving mesh method [37, 38], address this issue by dynamically clustering mesh points in critical regions using monitor functions (e.g., solution gradients or error estimates). Therefore, it is desirable to transfer such important and successful strategies to the field of neural-network-based solutions.

In this paper, we propose the Adaptive Feature Capture Method (AFCM), an extension of RFM that enhances resolution in high-gradient regions without increasing computational overhead. The AFCM leverages the gradient norm of an approximate solution to redistribute feature function hyperplanes and collocation points, concentrating them in regions of steep gradients. This adaptive refinement is iteratively applied until convergence, ensuring accurate approximations even for near-singular solutions. Crucially, AFCM preserves the mesh-free nature of RFM, making it suitable for complex geometries while maintaining computational efficiency. Numerical experiments validate the method’s effectiveness, demonstrating its potential for handling low-regularity PDEs.

The remainder of this paper is organized as follows: Section 2 introduces the RFM and TransNet initialization. Section 3 details the AFCM algorithm. Section 4 presents numerical experiments, and Section 5 concludes with remarks and future directions.

2. Random Feature Method and the General Neural Feature Space

2.1. Random Feature Method

Consider the following linear boundary-value problem

$$\begin{cases} \mathcal{L}\phi(\mathbf{x}) = \mathbf{f}(\mathbf{x}), & \mathbf{x} \in \Omega, \\ \mathcal{B}\phi(\mathbf{x}) = \mathbf{g}(\mathbf{x}), & \mathbf{x} \in \partial\Omega, \end{cases} \quad (1)$$

where Ω is a bounded spatial domain with the boundary $\partial\Omega$. The \mathcal{L} and \mathcal{B} are linear differential and boundary operators, respectively. We use d and d_ϕ to denote the dimensions of $\mathbf{x} = (x_1, x_2, \dots, x_d)$ and $\phi = (\phi_1, \phi_2, \dots, \phi_{d_\phi})$, respectively.

In RFM, the domain Ω is partitioned into M_p non-overlapping subdomains Ω_n , each centered at \mathbf{x}_n , such that $\Omega = \cup_{n=1}^{M_p} \Omega_n$. For each Ω_n , RFM applies a linear transformation

$$\tilde{\mathbf{x}} = \frac{1}{\mathbf{r}_n} (\mathbf{x} - \mathbf{x}_n), \quad n = 1, \dots, M_p, \quad (2)$$

to map Ω_n into $[-1, 1]^d$, where $\mathbf{r}_n \in R^d$ represents the radius of Ω_n . The PoU function ψ_n is defined such that $\text{supp}(\psi_n) = \Omega_n$. For $d = 1$, two commonly used PoU functions are

$$\psi_n(\mathbf{x}) = \mathbb{I}_{[-1,1]}(\tilde{\mathbf{x}}), \quad (3)$$

and

$$\begin{aligned} \psi_n(\mathbf{x}) = & \mathbb{I}_{[-\frac{5}{4}, -\frac{3}{4}]}(\tilde{\mathbf{x}}) \frac{1 + \sin(2\pi\tilde{\mathbf{x}})}{2} + \mathbb{I}_{[-\frac{3}{4}, \frac{3}{4}]}(\tilde{\mathbf{x}}) \\ & + \mathbb{I}_{[\frac{3}{4}, \frac{5}{4}]}(\tilde{\mathbf{x}}) \frac{1 - \sin(2\pi\tilde{\mathbf{x}})}{2}, \end{aligned} \quad (4)$$

where $\mathbb{I}_{[a,b]}(\mathbf{x}) = 1, \mathbf{x} \in [a, b]$ and $a \leq b$. For $d > 1$, the PoU function $\psi_n(\mathbf{x})$ is defined as $\psi_n(\mathbf{x}) = \prod_{i=1}^d \psi_n(x_i)$.

Next, a random feature function φ_{nj} on Ω_n is constructed using a two-layer neural network

$$\varphi_{nj}(\mathbf{x}) = \sigma(\mathbf{W}_{nj} \cdot \tilde{\mathbf{x}} + b_{nj}), \quad j = 1, 2, \dots, J_n, \quad (5)$$

where σ is the nonlinear activation function. The \mathbf{W}_{nj} and b_{nj} are randomly generated from the uniform distribution $\mathbb{U}(-R_m, R_m)$ and then fixed. The

R_m controls the magnitude of the parameters, and J_n is the number of random feature functions. The approximate solution in RFM is formed by a linear combination of the random feature functions and the PoU functions as follows

$$\tilde{\phi}(\mathbf{x}) = \left(\sum_{n=1}^{M_p} \psi_n(\mathbf{x}) \sum_{j=1}^{J_n} u_{nj}^1 \varphi_{nj}^1(\mathbf{x}), \dots, \sum_{n=1}^{M_p} \psi_n(\mathbf{x}) \sum_{j=1}^{J_n} u_{nj}^{d_\phi} \varphi_{nj}^{d_\phi}(\mathbf{x}) \right)^T, \quad (6)$$

where $u_{nj}^i \in \mathbb{R}$ are unknowns to be determined, and $M = \sum_{n=1}^{M_p} J_n$ denotes the degree of freedom.

Then, the linear least-squares method is utilized to minimize the loss function defined by

$$\begin{aligned} \text{Loss}(\{u_{nj}^i\}) = & \sum_{n=1}^{M_p} \left(\sum_{q=1}^{Q_n} \left\| \boldsymbol{\lambda}_{n,q} \left(\mathcal{L} \tilde{\phi}(\mathbf{x}_q^n) - \mathbf{f}(\mathbf{x}_q^n) \right) \right\|_2^2 \right) \\ & + \sum_{n=1}^{M_p} \left(\sum_{\mathbf{x}_q^n \in \partial\Omega} \left\| \boldsymbol{\lambda}_{n,b} \left(\mathcal{B} \tilde{\phi}(\mathbf{x}_q^n) - \mathbf{g}(\mathbf{x}_q^n) \right) \right\|_2^2 \right). \end{aligned} \quad (7)$$

When employing the PoU function ψ_n defined in (3), the regularization terms must be added to the loss function (7) to ensure continuity between neighboring subdomains. In contrast, when utilizing the ψ_n defined in (4), the regularization terms are not required. The loss function (7) can be written in matrix form

$$\mathcal{A}\mathbf{U} = \mathbf{f}, \quad (8)$$

where \mathcal{A} is the coefficient matrix related to both $\mathcal{L} \tilde{\phi}(\mathbf{x}_q^n)$ and $\mathcal{B} \tilde{\phi}(\mathbf{x}_q^n)$, \mathbf{f} is the right-hand side term associated with $\mathbf{f}(\mathbf{x}_q^n)$ and $\mathbf{g}(\mathbf{x}_q^n)$. To find the optimal parameter set $\mathbf{U} = (u_{nj}^i)^T$, the RFM samples Q_n collocation points $\{\mathbf{x}_q^n\}_{q=1}^{Q_n}$ within each subdomain Ω_n . It then calculates the rescaling parameters $\boldsymbol{\lambda}_{n,q} = \text{diag}(\lambda_{n,q}^1, \dots, \lambda_{n,q}^{d_\phi})$ and $\boldsymbol{\lambda}_{n,b} = \text{diag}(\lambda_{n,b}^1, \dots, \lambda_{n,b}^{d_\phi})$. Specifically,

the rescaling parameters are determined through the following formulas

$$\begin{aligned}
\lambda_{n,q}^i &= \frac{c}{\max_{1 \leq j \leq J_n} |\mathcal{L}(\psi_n(\mathbf{x}_q^n) \varphi_{nj}^i(\mathbf{x}_q^n))|}, \\
q &= 1, \dots, Q_n, \quad n = 1, \dots, M_p, \quad i = 1, \dots, d_\phi, \\
\lambda_{n,b}^i &= \frac{c}{\max_{1 \leq j \leq J_n} |\mathcal{B}(\psi_n(\mathbf{x}_q^n) \varphi_{nj}^i(\mathbf{x}_q^n))|}, \\
\mathbf{x}_q^n &\in \partial\Omega, \quad n = 1, \dots, M_p, \quad i = 1, \dots, d_\phi,
\end{aligned} \tag{9}$$

where $c > 0$ is a constant. Finally, the numerical result is obtained using equation (6).

Remark 1. (Nonlinear PDEs) When either the operator \mathcal{L} , the operator \mathcal{B} , or both are nonlinear, we opt to embed the least squares problem (8) into a nonlinear iterative solver, such as Picard's iterative method [39], for solving the PDE. In each iteration, the PDE is linearized, allowing the coefficient \mathbf{U} to be updated by solving (8) via the linear least-squares method.

2.2. The Construction of the Neural Feature Space

We follow the approach in [40]. For simplicity, let's assume Ω_n to be the unit ball $B_1(0)$. For regions of other shapes and sizes, the target region can be embedded within the unit ball $B_1(0)$ via simple translations and scaling operations. The random feature function φ_{nj} on Ω_n is redefined as follows

$$\varphi_{nj}(\mathbf{x}) = \sigma(\mathbf{W}_{nj} \cdot \tilde{\mathbf{x}} + b_{nj}) = \sigma(\gamma_{nj}(\mathbf{a}_{nj} \cdot \tilde{\mathbf{x}} + r_{nj})), \quad j = 1, 2, \dots, J_n, \tag{10}$$

where $\tilde{\mathbf{x}}$ represents \mathbf{x} after the linear transformation (2), $\mathbf{a}_{nj} = \frac{\mathbf{W}_{nj}}{|\mathbf{W}_{nj}|}$, $r_{nj} = \frac{b_{nj}}{|\mathbf{W}_{nj}|}$ and $\gamma_{nj} = |\mathbf{W}_{nj}|$. The position of the partition hyperplane is determined by the location parameter $(\mathbf{a}_{nj}, r_{nj})$ as follows

$$\mathbf{a}_{nj} \cdot \tilde{\mathbf{x}} + r_{nj} = 0, \quad j = 1, 2, \dots, J_n, \tag{11}$$

where the unit vector \mathbf{a}_{nj} represents the normal direction of the partition hyperplane and $|r_{nj}|$ indicates its distance from the origin. The shape parameter γ_{nj} modulates the steepness of the pre-activation value $\gamma_{nj}(\mathbf{a}_{nj} \cdot \tilde{\mathbf{x}} + r_{nj})$ in the normal direction \mathbf{a}_{nj} .

We define the distance from a point \mathbf{x} to the partition hyperplane (11) of the random feature function φ_{nj} on Ω_n as

$$\text{dist}_j(\mathbf{x}) = |\mathbf{a}_{nj} \cdot \tilde{\mathbf{x}} + r_{nj}|, \quad j = 1, 2, \dots, J_n, \quad (12)$$

and the partition hyperplane density as

$$D_{J_n}^\tau(\mathbf{x}) = \frac{1}{J_n} \sum_{j=1}^{J_n} 1_{\text{dist}_j(\mathbf{x}) < \tau}(\mathbf{x}), \quad (13)$$

where $\tau > 0$ denotes the bandwidth for density estimation, and $1_{\text{dist}_j(\mathbf{x}) < \tau}(\mathbf{x})$ represents the indicator function evaluating whether the distance between \mathbf{x} and the partition hyperplane of the random feature function φ_{nj} on Ω_n satisfies $\text{dist}_j(\mathbf{x}) < \tau$. The $D_{J_n}^\tau(\mathbf{x})$ quantifies the proportion of the random feature functions whose partition hyperplanes intersect the ball $B_\tau(\mathbf{x})$, centered at \mathbf{x} with radius τ .

In solving PDEs, the distribution of partition hyperplanes (11) within Ω_n can be controlled. For example, in TransNet, uniform distribution of partition hyperplanes is preferred. The location parameters $(\mathbf{a}_{nj}, r_{nj})$ are randomly chosen as

$$\mathbf{a}_{nj} = \frac{\mathbf{X}_{nj}}{|\mathbf{X}_{nj}|} \text{ and } r_{nj} = D_{nj}, \quad j = 1, 2, \dots, J_n, \quad (14)$$

where \mathbf{X}_{nj} is distributed as a d -dimensional standard Gaussian distribution, and D_{nj} follows a uniform distribution over $[0, 1]$. This sampling method generates a set of uniformly distributed partition hyperplanes (11) in Ω_n . For a fixed $\tau \in (0, 1)$, the expectation has $\mathbb{E}[D_{J_n}^\tau(\mathbf{x})] = \tau$ when $|\tilde{\mathbf{x}}| \leq 1 - \tau$.

TransNet also adopts the same shape parameter $\gamma_{nj} = \gamma_n$ for all random feature functions φ_{nj} defined on Ω_n . To compute the optimal shape parameter γ_n , L realizations of the Gaussian random fields (GRFs) $G(\mathbf{x} \mid \omega_l, \eta)_{l=1}^L$ are simulated, where ω_l denotes abstract randomness and η represents a fixed correlation length. The fitting error for each realization of GRFs and the approximate solution on Ω_n is defined as

$$\text{Loss}_l^{\gamma_n} = \min_{\{u_{nj}\}} \left(\sum_{q=1}^{Q_n} \left\| \sum_{j=1}^{J_n} u_{nj} \sigma(\gamma_n(\mathbf{a}_{nj} \cdot \tilde{\mathbf{x}}_q^n + r_{nj})) - G(\mathbf{x}_q^n \mid \omega_l, \eta) \right\|_2^2 \right). \quad (15)$$

The optimal shape parameter $\gamma_n = \gamma_n^{opt}$ is obtained by

$$\gamma_n^{opt} = \arg \min_{\gamma_n} \frac{1}{L} \sum_{l=1}^L \text{Loss}_l^{\gamma_n}, \quad (16)$$

which can be solved via grid search.

3. The Adaptive Feature Capture Method

We now present the Adaptive Feature Capture Method (AFCM). For the boundary value problem in Equation (1), we first partition the domain Ω into M_p non-overlapping subdomains $\{\Omega_n\}_{n=1}^{M_p}$. Within each Ω_n , we sample Q_n collocation points $\{\mathbf{x}_q^n\}_{q=1}^{Q_n}$ and construct J_n feature functions $\{\varphi_{nj}\}_{j=1}^{J_n}$ using the methodology described in Section 2.2. We employ the partition of unity (PoU) function ψ_n defined in Equation (3). The total number of feature functions is denoted as $J = \sum_{n=1}^{M_p} J_n$. To ensure continuity between subdomains, regularization terms enforcing C^1 continuity conditions at interfaces are added to the loss function (7) following the approach in [30]. The loss matrix (8) is then assembled and solved via linear least squares to obtain an initial approximate solution $\tilde{\phi}(\mathbf{x})$.

The accuracy of this initial solution $\tilde{\phi}(\mathbf{x})$ depends on the solution's regularity. While satisfactory for smooth solutions, its performance degrades significantly for low-regularity problems with steep gradients. This limitation arises because uniformly distributed partition hyperplanes and collocation points in the Random Feature Method (RFM) lack sufficient local expressive power in high-gradient regions. To address this, the AFCM adaptively increases feature function density and collocation point concentration in critical areas while preserving computational efficiency. The adaptation process consists of two key components:

Step 1: Feature Function Adaptation

We enhance the density of partition hyperplanes and the steepness of feature function pre-activations in high-gradient regions by adjusting the shape parameter γ_{nj} and location parameters $(\mathbf{a}_{nj}, r_{nj})$, using the gradient norm $|\nabla \tilde{\phi}(\mathbf{x})|$ as an indicator. We first uniformly sample m points S across Ω and define a probability density function (PDF) on S :

$$p(\mathbf{x}) = \frac{(|\nabla \tilde{\phi}(\mathbf{x})| + c_1)}{\sum_{\mathbf{x} \in S} (|\nabla \tilde{\phi}(\mathbf{x})| + c_1)}, \quad \mathbf{x} \in S, \quad (17)$$

where $c_1 > 0$ prevents excessive concentration. From this PDF, we sample J points via weighted random sampling (WRS) without replacement from the set S , with $\{\mathbf{x}_j^n\}_{j=1}^{J'_n}$ denoting points in Ω_n (note that J'_n is usually different from J_n), where the weights for sampling are determined by the PDF. The feature functions on Ω_n are reconstructed via:

$$\gamma_{nj} = \gamma_n \cdot \frac{(|\nabla \tilde{\phi}(\mathbf{x}_j^n)| + c_2)}{\min_{\mathbf{x} \in \{\mathbf{x}_j^n\}_{j=1}^{J'_n}} (|\nabla \tilde{\phi}(\mathbf{x})| + c_2)}, \quad j = 1, \dots, J'_n, \quad (18)$$

$$\mathbf{a}_{nj} = \frac{\mathbf{X}_{nj}}{|\mathbf{X}_{nj}|}, \quad r_{nj} = -\mathbf{a}_{nj} \cdot \tilde{\mathbf{x}}_j^n, \quad j = 1, \dots, J'_n, \quad (19)$$

where γ_n is the initial shape parameter from Equations (15)–(16), \mathbf{X}_{nj} follows a d -dimensional standard Gaussian distribution, and $c_2 > 0$ controls shape parameter variation to avoid numerical instability.

During the adaptation process, Equation (18) determines the shape parameter γ_{nj} at each sampling point \mathbf{x}_j^n by scaling the initial constant γ_n proportionally to the local gradient magnitude $|\nabla \tilde{\phi}(\mathbf{x}_j^n)|$. This proportional scaling ensures feature functions become steeper in high-gradient regions while maintaining moderate variations elsewhere. Specifically, locations with larger solution gradients receive amplified γ_{nj} values, enhancing local approximation capability without global parameter modifications.

Equation (19) geometrically enforces that each feature function's partition hyperplane intersects its corresponding sampling point \mathbf{x}_j^n . This critical constraint ensures the adapted basis functions remain anchored to regions requiring enhanced resolution, creating a dynamic alignment between network architecture and solution characteristics.

Step 2: Collocation Point Adaptation

Interior collocation points are redistributed to high-gradient regions using the same PDF $p(\mathbf{x})$. We sample $\sum_{n=1}^{M_p} I_n$ points via WRS without replacement from the set S , with $\{\mathbf{x}_i^n\}_{i=1}^{I'_n}$ denoting interior points in Ω_n , where the weights for sampling are determined by the PDF. The updated collocation points on Ω_n become:

$$\{\mathbf{x}_q^n \mid \mathbf{x}_q^n \in \partial\Omega_n\} \cup \{\mathbf{x}_i^n\}_{i=1}^{I'_n}. \quad (20)$$

After these adaptations, the loss matrix (8) is reassembled and solved to obtain an improved approximation $\tilde{\phi}(\mathbf{x})$. The AFCM iteratively applies this

Algorithm 1 The Adaptive Feature Capture Method

Input: • Number of subdomains M_p

- Number of feature functions per subdomain J_n
- Number of collocation points per subdomain Q_n
- Number of interior collocation points per subdomain I_n
- Rescaling parameter c , coefficients c_1, c_2
- Number of iterations K
- Number of sampling points m
- Number of GRF realizations L
- Correlation length ℓ_η

Output: The K -th approximate solution $\tilde{\phi}(\mathbf{x})$;

Divide Ω into M_p non-overlapping subdomains Ω_n ;

for $k = 0$ **do**

1. Sample Q_n collocation points $\{\mathbf{x}_q^n\}_{q=1}^{Q_n}$ in each Ω_n ;
2. Generate J_n location parameters $\{(\mathbf{a}_{nj}, r_{nj})\}_{j=1}^{J_n}$ on Ω_n according to (14);
3. Compute the shape parameter γ_n on Ω_n according to (15) and (16);
4. Construct J_n feature functions $\{\varphi_{nj}\}_{j=1}^{J_n}$ on Ω_n by (10);
5. Assemble the loss matrix (8) and solve it by the linear least-squares method to obtain the k -th approximate solution $\tilde{\phi}(\mathbf{x})$;

end for

Sample m points S in the entire Ω by the uniform distribution;

for $k = 1, 2, \dots, K$ **do**

1. Define PDF $p(\mathbf{x})$ for the points S according to (17);
2. Sample $\sum_{n=1}^{M_p} J_n$ points from S according to $p(\mathbf{x})$ and reconstruct the feature functions $\{\varphi_{nj}\}_{j=1}^{J'_n}$ on Ω_n by (18) and (19)
3. Sample $\sum_{n=1}^{M_p} I_n$ points from S according to $p(\mathbf{x})$ and regenerate the collocation points on Ω_n according to (20).
4. Assemble the loss matrix (8) and solve it by the linear least-squares method to obtain the k -th approximate solution $\tilde{\phi}(\mathbf{x})$;

end for

Return the K -th approximate solution $\tilde{\phi}(\mathbf{x})$.

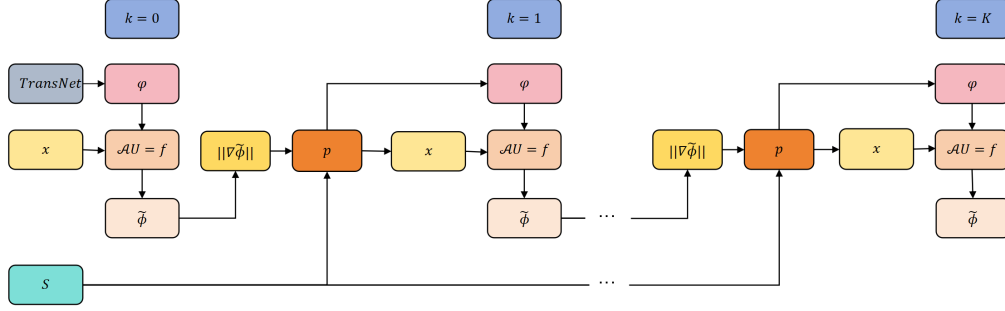


Figure 1: The computational framework of of Algorithm 1.

process until convergence, as formalized in Algorithm 1. Figure 1 illustrates the computational framework.

This adaptive strategy ensures that partition hyperplanes and collocation points cluster in critical regions, achieving enhanced resolution without increasing computational overhead. The mesh-free nature of RFM is preserved, making AFCM suitable for complex geometries while maintaining efficiency.

4. Numerical Experiments

We present numerical experiments to validate the proposed method. The relative L^∞ and L^2 error norms between the numerical solution $\tilde{\phi}_k(\mathbf{x})$ and exact solution $\phi(\mathbf{x})$ are defined as:

$$\|e_k\|_{L^\infty} = \frac{\|\tilde{\phi}_k(\mathbf{x}) - \phi(\mathbf{x})\|_{L^\infty}}{\|\phi(\mathbf{x})\|_{L^\infty}}, \quad \|e_k\|_{L^2} = \frac{\|\tilde{\phi}_k(\mathbf{x}) - \phi(\mathbf{x})\|_{L^2}}{\|\phi(\mathbf{x})\|_{L^2}} \quad (21)$$

where $k = 0, \dots, K$ denotes the number of adaptive iterations. For $d = 2$, we set $M_p = N_x \times N_y$ and $Q_n = Q_x \times Q_y$, where N_x, N_y represent subdomain counts and Q_x, Q_y collocation points per subdomain. Figure 2 shows the initial subdomain arrangement and collocation point distribution.

All linear least squares computations use PyTorch's `torch.linalg.lstsq` solver. Key experimental parameters are summarized in Table 1

4.1. Two-Dimensional Poisson equation with a near singular solution with one peak

We consider the Poisson equation on $\Omega = (-1, 1)^2$:

$$\begin{cases} -\Delta \phi(x, y) = f(x, y), & (x, y) \in \Omega \\ \phi(x, y) = g(x, y), & (x, y) \in \partial\Omega \end{cases} \quad (22)$$

Table 1: Parameters and experimental configurations for numerical experiments

number of the subdomains $M_p = N_x \times N_y$	3×3
number of the collocation points in each subdomain $Q_n = Q_x \times Q_y$	79×79
number of the interior collocation points in each subdomain I_n	77×77
constant coefficient of the rescaling parameters c	1
number of the realizations of the GRFs L	10
constant c_1	0.01
constant c_2	50
bandwidth for the density τ	0.2
correlation length η	0.5
activation function σ	\tanh^3
CPU	Intel Xeon Platinum 8358
GPU	NVIDIA A100 (80GB)

with exact solution containing a peak at $(0, 0)$ and very large solution variation near $(0, 0)$:

$$\phi(x, y) = e^{-1000(x^2+y^2)} \quad (23)$$

The source term $f(x, y)$ and boundary condition $g(x, y)$ are derived directly from (22)–(23). Using $m = 1.26 \times 10^6$ sampling points, we obtain adaptive solutions via Algorithm 1. We show in Table 2 the relative errors for $\phi(x, y)$

Table 2: The initial shape parameter γ_n and the relative errors for (23) with different J_n at $k = 0$ and $k = K = 4$ iterations

m	J_n	1500	2000	3000	4000
	γ_n	2.0	2.6	2.8	3.4
1.26×10^6	$\ e_0\ _{L^\infty}$	9.79E-2	2.55E-1	8.26E-2	7.81E-2
	$\ e_0\ _{L^2}$	2.50E-1	1.02E-0	2.70E-1	2.48E-1
	$\ e_{K=4}\ _{L^\infty}$	2.48E-5	1.19E-8	1.02E-9	6.45E-11
	$\ e_{K=4}\ _{L^2}$	3.83E-5	2.11E-8	2.99E-9	1.38E-10

at the initial iteration ($k = 0$) and the final iteration ($k = 4$) and for different J_n . The results demonstrates significant error reduction through adaptive iterations, with monotonic decay as J_n increases. For $J_n = 4000$, we show in

Figure 3 that

- The exact solution ϕ and approximate solutions $\tilde{\phi}_k$ on Ω
- Relative errors $\|e_k\|_{L^\infty}$ and $\|e_k\|_{L^2}$
- local surfaces of approximate solutions $\tilde{\phi}_k$ on $[-0.1, 0.1]^2$

Figure 4 illustrates the evolution of partition hyperplanes, collocation points, and shape parameters. Key observations include:

- Increased spatial concentration of collocation points after adaptation
- Magnified shape parameters in regions with steep gradients
- Stabilized error convergence after 4 iterations

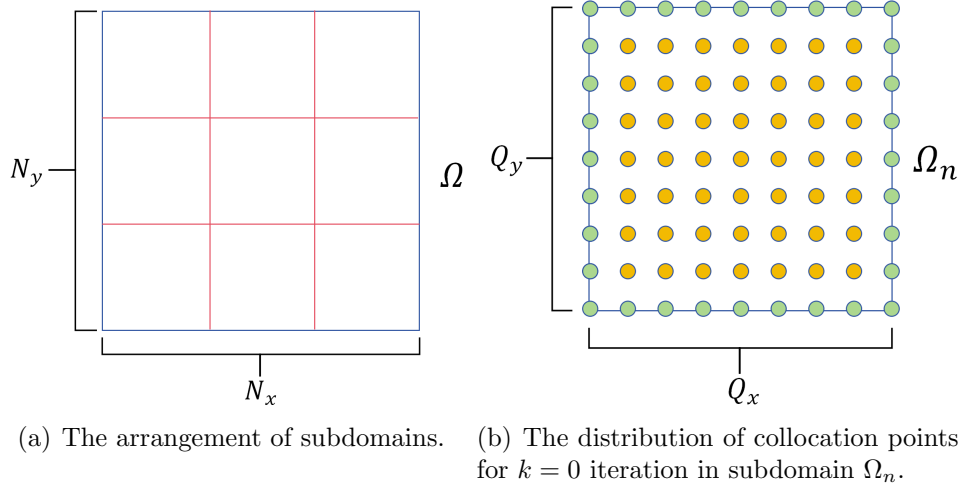


Figure 2: The arrangement of subdomains and the distribution of collocation points for $k = 0$ iteration in subdomain Ω_n . (a) The blue lines and red lines represent the boundaries and the interfaces between subdomains, respectively. (b) The green points and yellow points represent the boundary points and interior points in each subdomain, respectively.

These results confirm our method's effectiveness in resolving sharp solution features through adaptive feature capture.

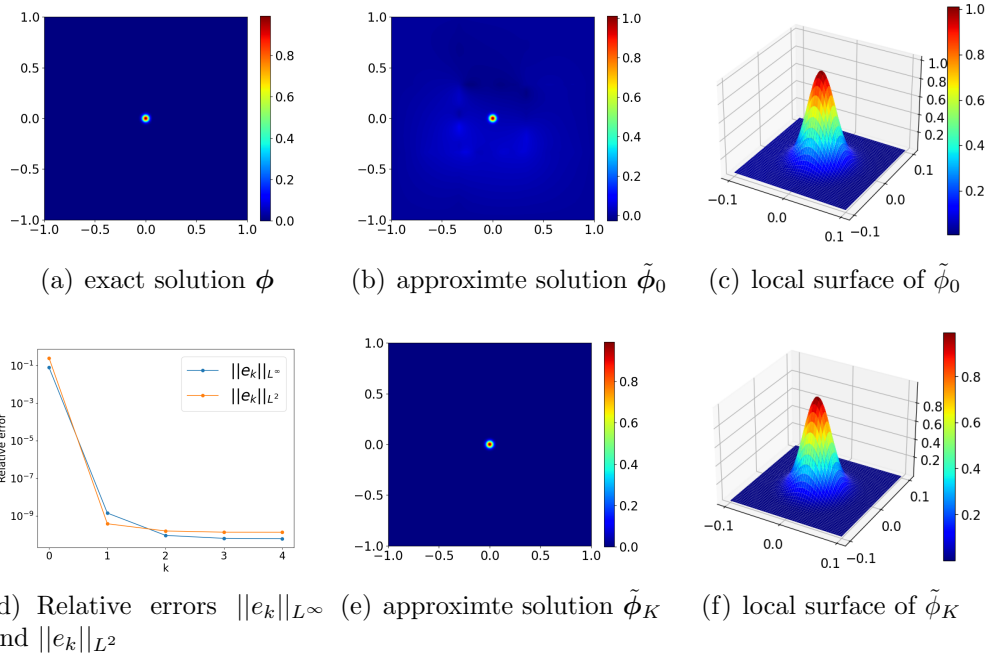
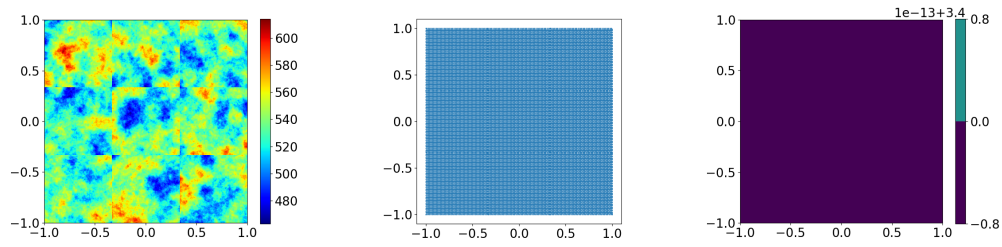
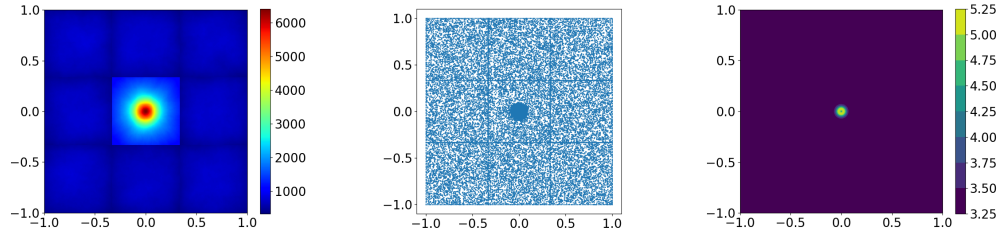


Figure 3: The exact solution and the numerical results for (23) with $J_n = 4000$ and $K = 4$.



(a) partition hyperplane density ($k = 0$) (b) collocation points ($k = 0$) (c) shape parameter ($k = 0$)



(d) partition hyperplane density ($k = K$) (e) collocation points ($k = K$) (f) shape parameter ($k = K$)

Figure 4: The partition hyperplane density, the collocation points and the shape parameters for (23) with $J_n = 4000$ at $k = 0$ and $k = K = 4$ iterations.

4.2. Two-Dimensional Poisson equation with a near singular solution with two peaks

Consider the two-dimensional Poisson equation (22) in $\Omega = (-1, 1)^2$, the exact solution with two peaks is given by

$$\phi(x, y) = e^{-1000(x^2 + (y - \frac{2}{3})^2)} + e^{-1000(x^2 + (y + \frac{2}{3})^2)}. \quad (24)$$

The Dirichlet boundary condition $g(x, y)$ and source term $f(x, y)$ are directly derived from this analytical solution. We implement Algorithm 1 with $m = 1.26 \times 10^6$ sampling points to resolve the steep gradients near $(0, \pm \frac{2}{3})$.

Table 3 summarizes the numerical performance across different feature function densities (J_n), showing both initial ($k = 0$) and adapted ($k = 4$) solution errors. The adaptation process reduces relative errors by up to 10 orders of magnitude, demonstrating AFCM's effectiveness in handling dual near-singularities. Notably, the L^∞ error decreases from 1.18×10^{-1} to 4.10×10^{-5} for $J_n = 1500$, and achieves machine-precision-level accuracy (1.07×10^{-10}) for $J_n = 4000$.

Figure 5 illustrates the solution evolution through adaptation iterations, comparing the exact solution $\phi(x, y)$ with numerical approximations $\tilde{\phi}_k$ at $k = 0$ and $k = 4$. Figure 6 further demonstrates the adaptive redistribution process, showing increased partition hyperplane density and collocation point concentration around both peaks, accompanied by appropriately scaled shape parameters in high-gradient regions.

Table 3: The initial shape parameter γ_n and the relative errors for (24) with different J_n at $k = 0$ and $k = K = 4$ iterations

m	J_n	1500	2000	3000	4000
	γ_n	2.0	2.6	2.8	3.4
1.26×10^6	$\ e_0\ _{L^\infty}$	1.18E-1	1.08E-1	5.93E-2	1.82E-1
	$\ e_0\ _{L^2}$	1.64E-1	2.48E-1	1.31E-1	4.65E-1
	$\ e_{K=4}\ _{L^\infty}$	4.10E-5	9.79E-9	1.75E-9	1.07E-10
	$\ e_{K=4}\ _{L^2}$	6.75E-5	1.28E-8	2.02E-9	9.76E-11

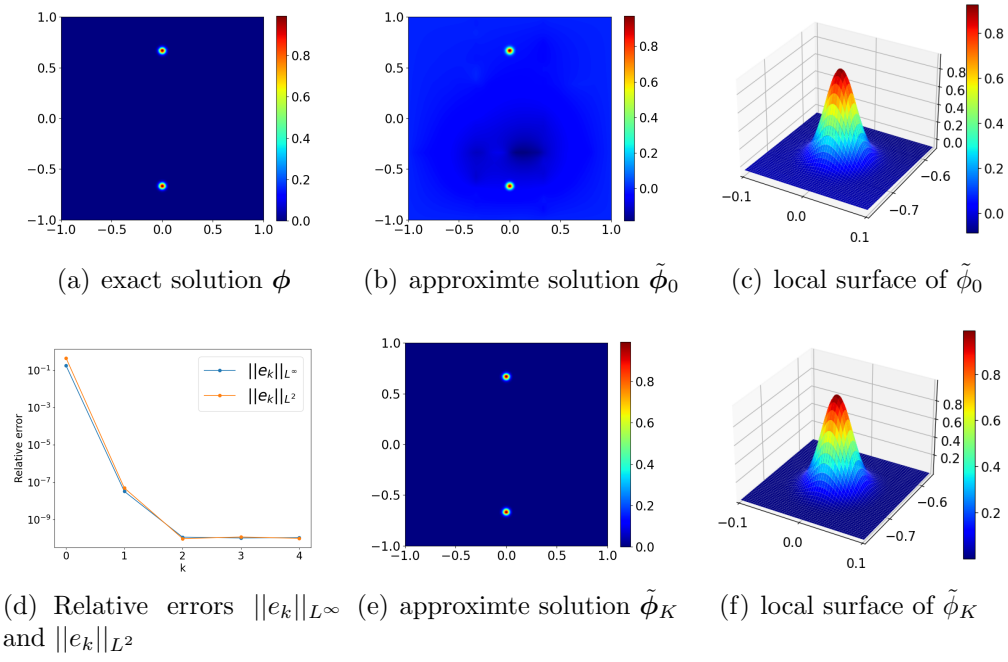
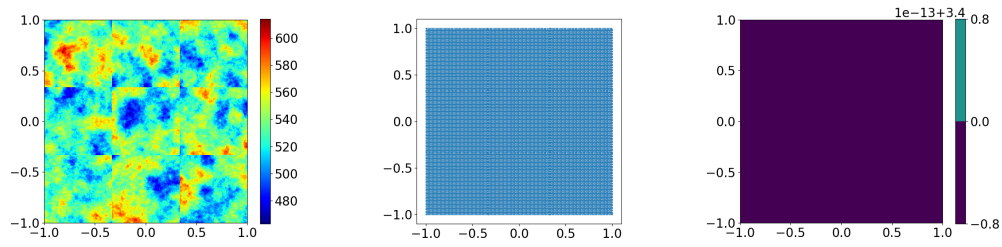
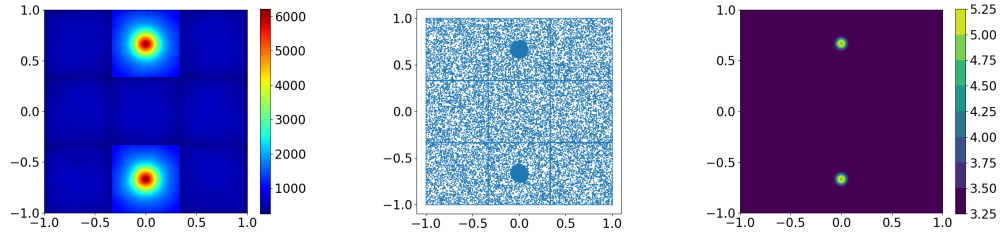


Figure 5: The exact solution and the numerical results for (24) with $J_n = 4000$ and $K = 4$.



(a) partition hyperplane density ($k = 0$) (b) collocation points ($k = 0$) (c) shape parameter ($k = 0$)



(d) partition hyperplane density ($k = K$) (e) collocation points ($k = K$) (f) shape parameter ($k = K$)

Figure 6: The partition hyperplane density, the collocation points and the shape parameters for (24) with $J_n = 4000$ at $k = 0$ and $k = K = 4$ iterations

4.3. Two-Dimensional Poisson Equation with Line Singularity

We examine a challenging case of the two-dimensional Poisson equation (21) on $\Omega = (-1, 1)^2$ featuring a solution with near-singular behavior concentrated along a line:

$$\phi(x, y) = e^{-1000\left(x - \frac{y}{20}\right)^2}. \quad (25)$$

The Dirichlet boundary condition $g(x, y)$ and source term $f(x, y)$ are directly derived from this analytical solution. With $m = 1.8 \times 10^5$ sampling points, we employ Algorithm 1 to resolve the steep gradient along the line $x = y/20$.

Table 4 demonstrates the significant error reduction achieved through adaptive refinement. After four iterations, the L^∞ error decreases from $\mathcal{O}(10^{-1})$ to $\mathcal{O}(10^{-10})$ for $J_n = 4000$, representing an improvement of seven orders of magnitude.

Figure 7 illustrates the solution characteristics and adaptation progress. Figure 8 further demonstrates the adaptive mechanism: partition hyperplanes become densely clustered along the singularity line, collocation points concentrate in the critical region, and shape parameters increase substantially to capture the steep gradient.

Table 4: The initial shape parameter γ_n and the relative errors for (25) with different J_n at $k = 0$ and $k = K = 4$ iterations

m	J_n	1500	2000	3000	4000
	γ_n	2.0	2.6	2.8	3.4
1.8×10^5	$\ e_0\ _{L^\infty}$	2.40E-1	3.30E-1	2.44E-1	9.17E-2
	$\ e_0\ _{L^2}$	2.25E-1	3.06E-1	3.17E-1	1.26E-1
	$\ e_{K=4}\ _{L^\infty}$	8.58E-6	4.54E-9	1.15E-9	1.50E-10
	$\ e_{K=4}\ _{L^2}$	8.00E-6	1.82E-9	1.09E-9	1.16E-10

4.4. Two-Dimensional Poisson Equation with Line Singularity

We examine a challenging case of the two-dimensional Poisson equation (21) on $\Omega = (-1, 1)^2$ featuring a solution with near-singular behavior concentrated along a line:

$$\phi(x, y) = e^{-7000\left(x - \frac{y}{20}\right)^2}. \quad (26)$$

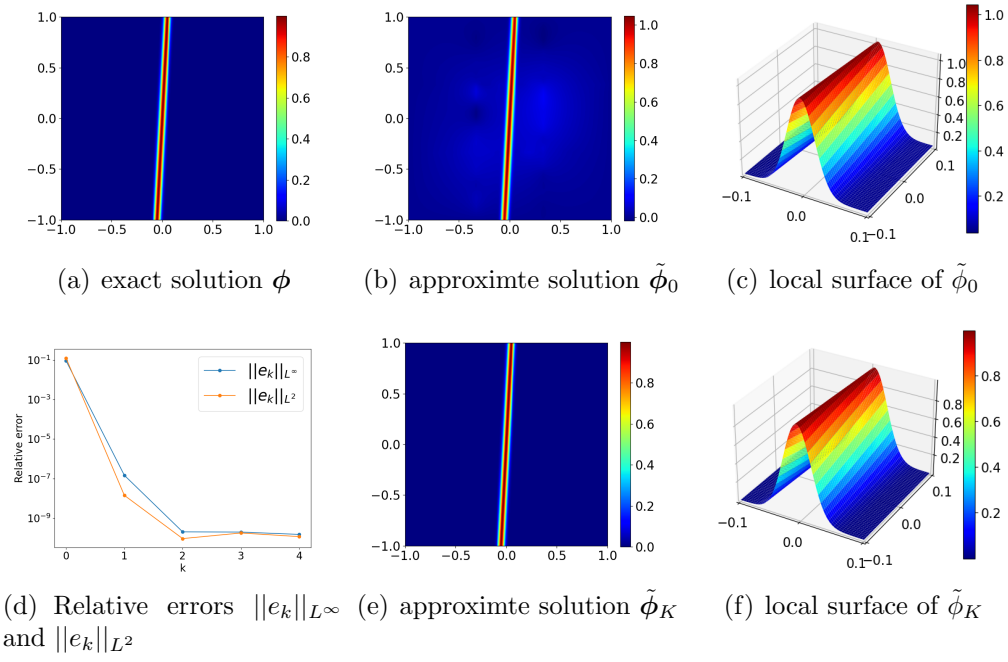
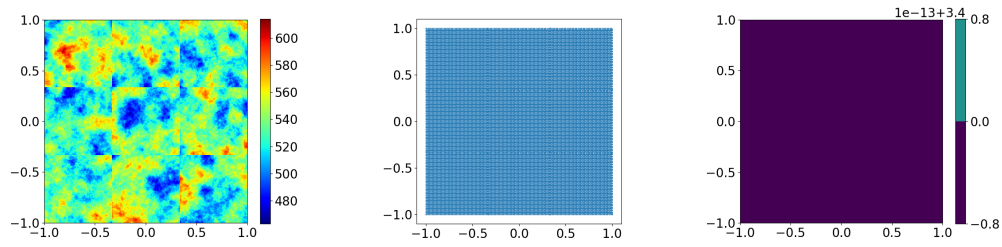
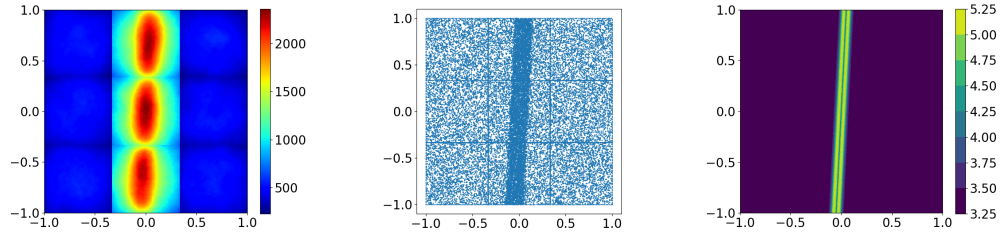


Figure 7: The exact solution and the numerical results for (25) with $J_n = 4000$ and $K = 4$.



(a) partition hyperplane density ($k = 0$) (b) collocation points ($k = 0$) (c) shape parameter ($k = 0$)



(d) partition hyperplane density ($k = K$) (e) collocation points ($k = K$) (f) shape parameter ($k = K$)

Figure 8: The partition hyperplane density, the collocation points and the shape parameters for (25) with $J_n = 4000$ at $k = 0$ and $k = K = 4$ iterations

The Dirichlet boundary condition $g(x, y)$ and source term $f(x, y)$ are directly derived from this analytical solution. With $M_p = N_x \times N_y = 9 \times 1$ subdomains and $m = 1.8 \times 10^5$ sampling points, we employ Algorithm 1 to resolve the steep gradient along the line $x = y/20$.

Table 5 demonstrates the significant error reduction achieved through adaptive refinement. After four iterations, the L^∞ error decreases from $\mathcal{O}(10^{-1})$ to $\mathcal{O}(10^{-11})$ for $J_n = 4000$, representing an improvement of seven orders of magnitude.

Figure 9 illustrates the solution characteristics and adaptation progress. Figure 10 further demonstrates the adaptive mechanism: partition hyper-planes become densely clustered along the singularity line, collocation points concentrate in the critical region, and shape parameters increase substantially to capture the steep gradient.

Table 5: The initial shape parameter γ_n and the relative errors for (26) with different J_n at $k = 0$ and $k = K = 4$ iterations

m	J_n	1500	2000	3000	4000
	γ_n	2.0	2.6	2.8	3.4
1.8×10^5	$\ e_0\ _{L^\infty}$	4.45E-1	5.83E-1	2.48E-1	2.50E-1
	$\ e_0\ _{L^2}$	6.08E-1	1.36E-0	5.58E-1	6.16E-1
	$\ e_{K=4}\ _{L^\infty}$	1.67E-9	1.69E-10	9.98E-11	5.88E-11
	$\ e_{K=4}\ _{L^2}$	1.45E-9	1.27E-10	7.65E-11	8.52E-11

4.5. One-dimensional Burgers equation with one line

Consider the one-dimensional Burgers equation defined on the computational domain $\Omega \times (0, T] = (0, 1) \times (0, 1]$,

$$\begin{cases} \phi_t(x, t) + \phi(x, t)\phi_x(x, t) - \epsilon\phi_{xx}(x, t) = f(x, t), & (x, t) \in \Omega \times (0, T], \\ \phi(x, t) = g(x, t), & (x, t) \in \partial\Omega \times (0, T], \\ \phi(x, 0) = h(x), & x \in \Omega, \end{cases} \quad (27)$$

the exact solution is given by

$$\phi(x, t) = \frac{1}{1 + e^{\frac{x-t}{2\epsilon}}}. \quad (28)$$

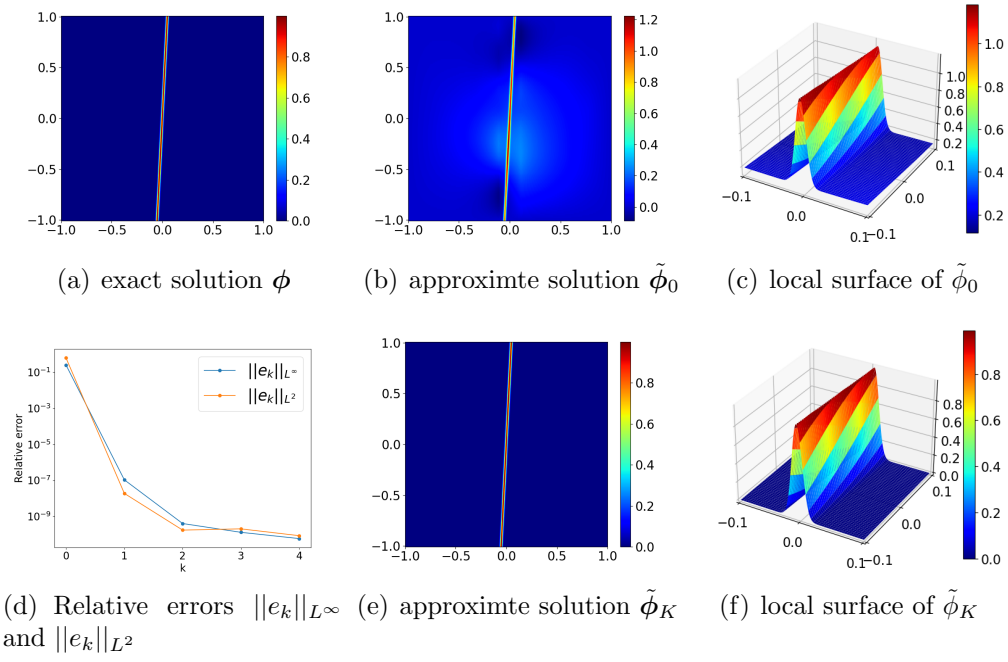
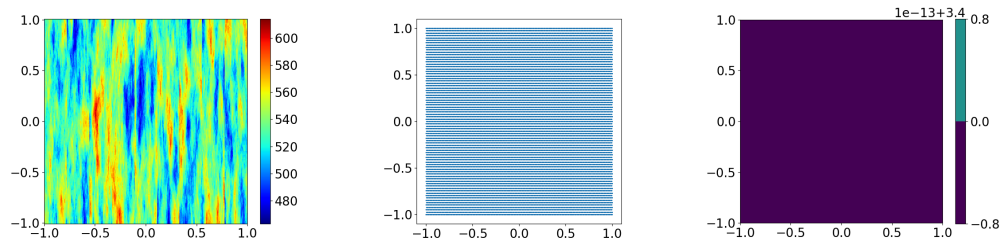
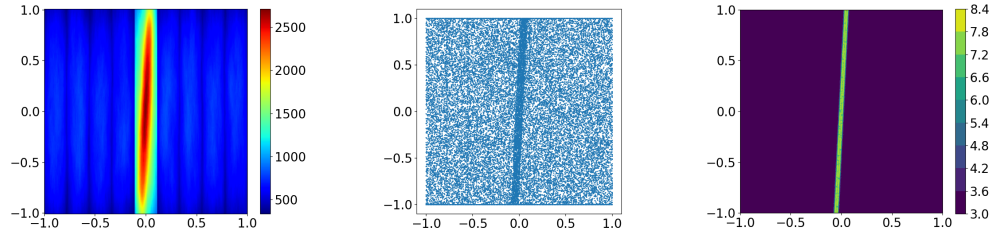


Figure 9: The exact solution and the numerical results for (26) with $J_n = 4000$ and $K = 4$.



(a) partition hyperplane density ($k = 0$) (b) collocation points ($k = 0$) (c) shape parameter ($k = 0$)



(d) partition hyperplane density ($k = K$) (e) collocation points ($k = K$) (f) shape parameter ($k = K$)

Figure 10: The partition hyperplane density, the collocation points and the shape parameters for (26) with $J_n = 4000$ at $k = 0$ and $k = K = 4$ iterations

The Dirichlet boundary condition $g(x, t)$ on $\partial\Omega \times (0, T]$, the initial condition $h(x)$ on Ω and the function $f(x, t)$ are given by the exact solution. For this case, we treat the time variable t as the spatial variable y . We set $\epsilon = 0.006$ and $m = 9.0 \times 10^4$. Algorithm 1 is employed to estimate $\phi(x, t)$. We utilize Picard's iterative methods to handle nonlinearity address nonlinearity, with the number of iterations set to 40. The initial shape parameter γ_n and the relative errors for $\phi(x, t)$ with different J_n at initial ($k = 0$) and final ($k = K = 4$) iterations are summarized in Table 6. For $J_n = 4000$, Figure 11 displays the exact solution ϕ , the relative errors $\|e_k\|_{L^\infty}$ and $\|e_k\|_{L^2}$, the approximate solutions $\tilde{\phi}_k$, and the local surfaces of approximate solution $\tilde{\phi}_k$ on $[0.4, 0.6]^2$ at the initial ($k = 0$) and final ($k = K = 4$) iterations. The partition hyperplane density, the collocation points and the shape parameters with $J_n = 4000$ at $k = 0$ and $k = K = 4$ iterations are shown in Figure 12.

Table 6: The initial shape parameter γ_n and the relative errors for (28) with different J_n at $k = 0$ and $k = K = 4$ iterations

m	J_n	1500	2000	3000	4000
	γ_n	2.0	2.6	2.8	3.4
9.0×10^4	$\ e_0\ _{L^\infty}$	1.04E-2	1.60E-2	3.45E-2	4.48E-1
	$\ e_0\ _{L^2}$	2.51E-3	4.10E-3	9.66E-3	8.97E-2
	$\ e_{K=4}\ _{L^\infty}$	1.16E-2	3.20E-4	1.46E-5	5.77E-6
	$\ e_{K=4}\ _{L^2}$	6.58E-4	2.40E-5	3.40E-6	3.91E-7

4.6. Two-dimensional Heat equation with one peak

Consider the two-dimensional Heat equation in $\Omega \times (0, T] = (-1, 1)^2 \times (0, 2]$,

$$\begin{cases} \phi_t(x, y, t) - \alpha \Delta \phi(x, y, t) = f(x, y, t), & (x, y, t) \in \Omega \times (0, T], \\ \phi(x, y, t) = g(x, y, t), & (x, y, t) \in \partial\Omega \times (0, T], \\ \phi(x, y, 0) = h(x, y), & (x, y) \in \Omega, \end{cases} \quad (29)$$

the exact solution is given by

$$\phi(x, y, t) = e^{-1000((x-\frac{t}{10})^2 + (y-\frac{t}{10})^2)}. \quad (30)$$

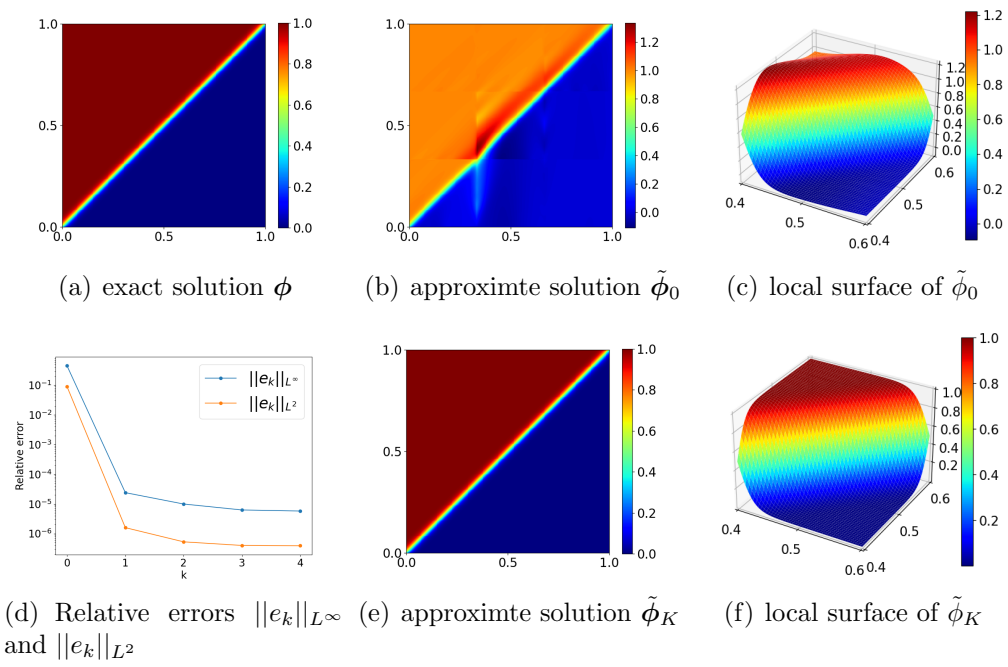
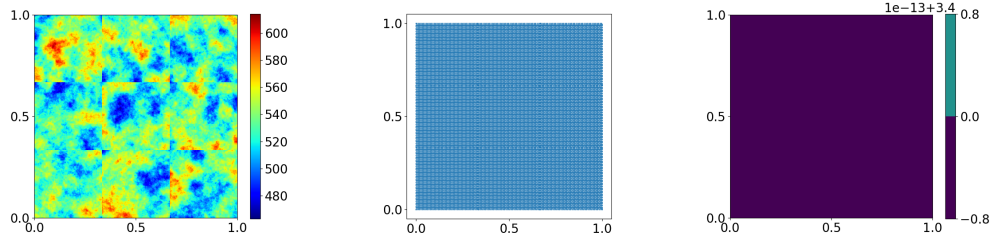
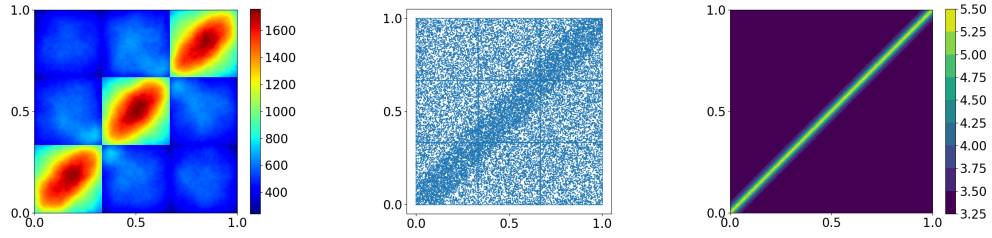


Figure 11: The exact solution and the numerical results for (28) with $J_n = 4000$ and $K = 4$.



(a) partition hyperplane density ($k = 0$) (b) collocation points ($k = 0$) (c) shape parameter ($k = 0$)



(d) partition hyperplane density ($k = K$) (e) collocation points ($k = K$) (f) shape parameter ($k = K$)

Figure 12: The partition hyperplane density, the collocation points and the shape parameters for (28) with $J_n = 4000$ at $k = 0$ and $k = K = 4$ iterations

The Dirichlet boundary condition $g(x, y, t)$ on $\partial\Omega \times (0, T]$, the initial condition $h(x, y)$ on Ω and the function $f(x, y, t)$ are given by the exact solution. For this example, we use the Crank-Nicolson scheme for time discretization and apply the AFCM with K adaptive iterations at each time step. The collocation points and feature functions after the adaptation of the previous time step are used as the initial collocation points and feature functions of the next time step. We set $\alpha = 1000$, the number of time steps $N = 10$, the time interval $dt = 0.2$, $m = 1.26 \times 10^6$ and Algorithm 1 is employed to estimate $\phi(x, y, t)$. The initial shape parameter γ_n and the relative errors for $\phi(x, y, t)$ at the final ($k = K$) iteration and $T = 2.0$ with $K = 0, 4$ and different J_n are summarized in Table 7. For $J_n = 4000$, Figure 13 and Figure 14 display the exact solution ϕ , the approximate solutions $\tilde{\phi}_k$, and the local surfaces of approximate solution $\tilde{\phi}_k$ on $[\frac{t}{10} - 0.1, \frac{t}{10} + 0.1]^2$ at the final ($k = K$) iteration and $t = 0.2, 1.0, 2.0$ with $K = 0, 4$. The partition hyperplane density, the collocation points and the shape parameters with $K = 4$ and $J_n = 4000$ at the final ($k = K$) iteration and $t = 0.2, 1.0, 2.0$ are shown in Figure 15, which shows that the positions of the concentration of the partition hyperplane and the collocation points, as well as the positions of the changes in the shape parameters, move with the shift of the peak position of the solution.

Table 7: The initial shape parameter γ_n and the relative errors for (30) at the final ($k = K$) iteration and $T = 1.0$ with $K = 0, 4$ and different J_n

T	m	J_n	1500	2000	3000	4000
		γ_n	2.0	2.6	2.8	3.4
2.0	1.26×10^6	$\ e_{K=0}\ _{L^\infty}$	8.22E-2	8.42E-2	2.44E-2	3.17E-2
		$\ e_{K=0}\ _{L^2}$	1.46E-1	2.93E-1	7.78E-2	1.06E-1
		$\ e_{K=4}\ _{L^\infty}$	2.67E-5	5.36E-7	4.34E-7	4.20E-7
		$\ e_{K=4}\ _{L^2}$	4.45E-5	7.22E-7	4.65E-7	4.68E-7

4.7. Two-dimensional Convection-Diffusion equation with one line

Consider the two-dimensional Convection-Diffusion equation defined on the computational domain $\Omega = (0, 1)^2$,

$$\begin{cases} -\varepsilon \Delta \phi(x, y) + b \cdot \nabla \phi(x, y) = f(x, y), & (x, y) \text{ in } \Omega, \\ \phi(x, y) = g(x, y), & (x, y) \text{ on } \partial\Omega, \end{cases} \quad (31)$$

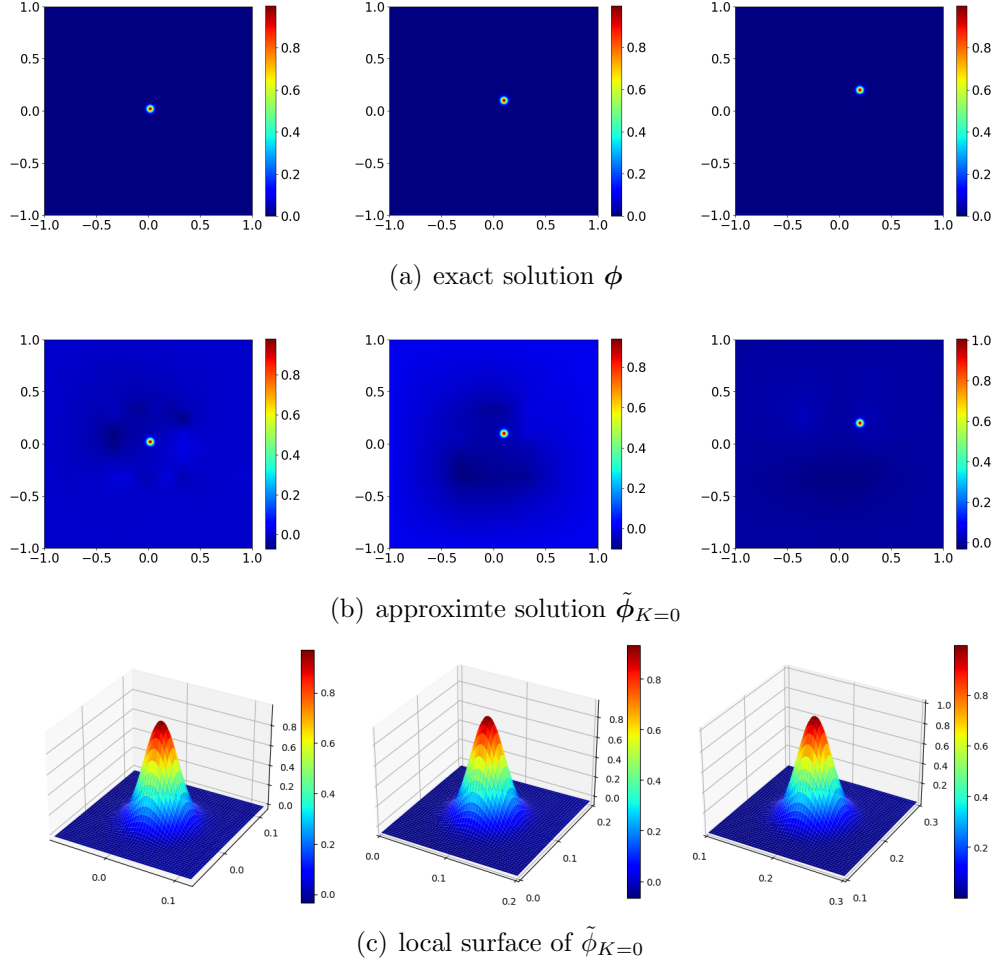


Figure 13: The exact solution and the numerical results for (30) at the final ($k = K$) iteration and $t = 0.2$ (left), 1.0 (middle), 2.0 (left) with $J_n = 4000$ and $K = 0$.

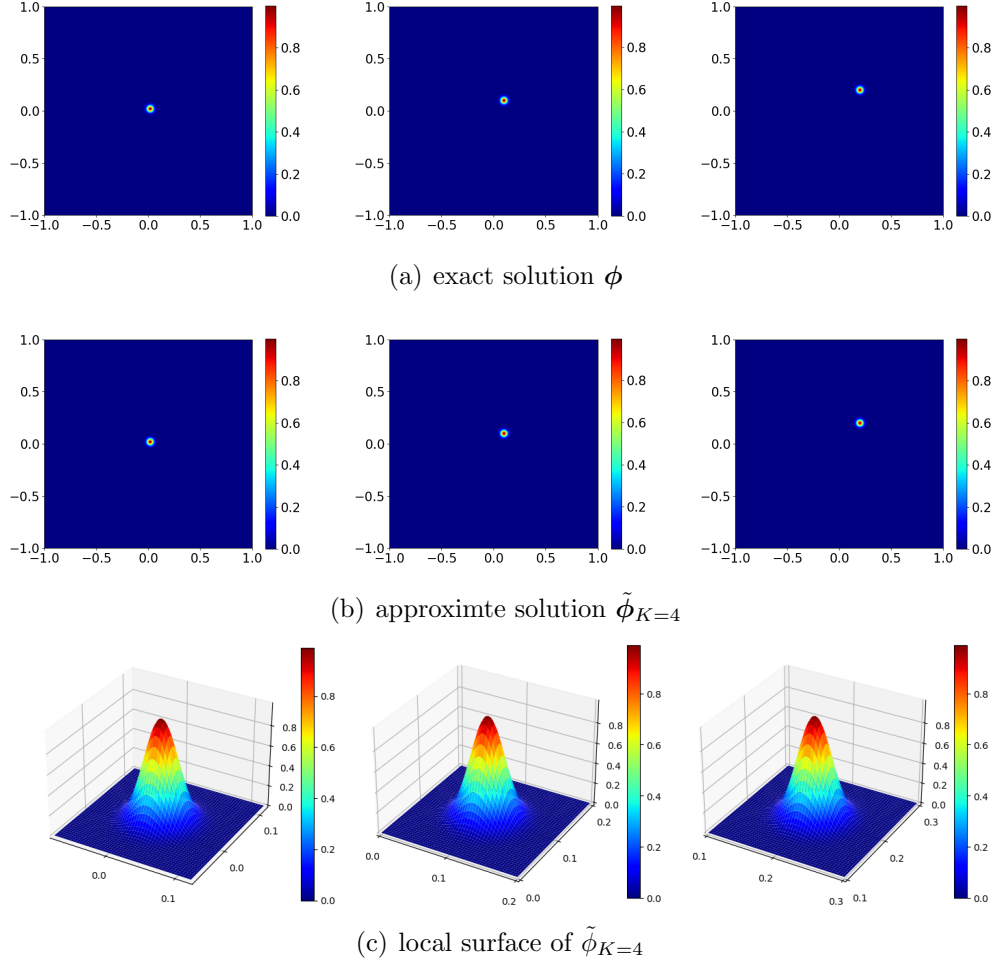
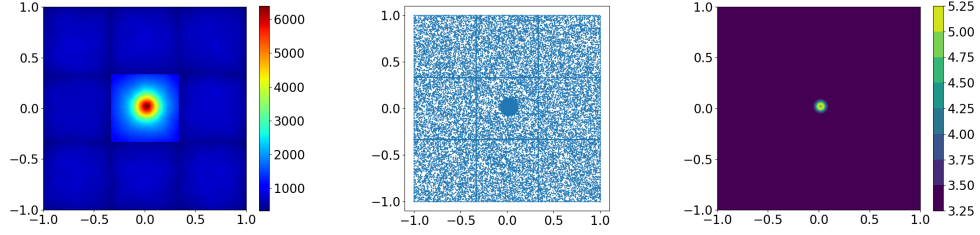
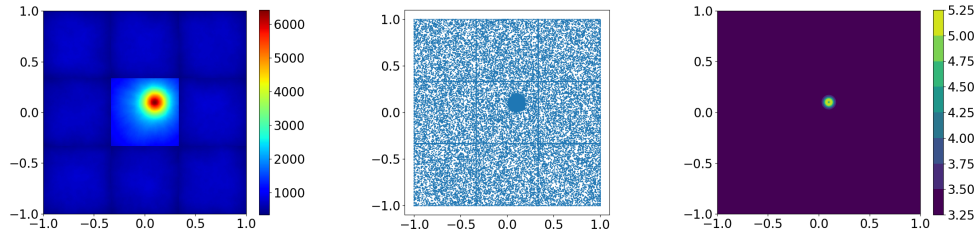


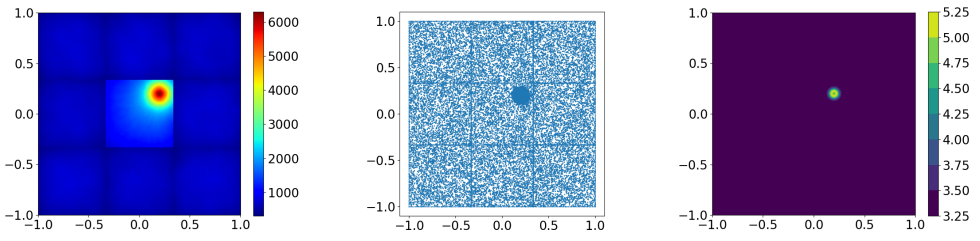
Figure 14: The exact solution and the numerical results for (30) at the final ($k = K$) iteration and $t = 0.2$ (left), 1.0 (middle), 2.0 (left) with $J_n = 4000$ and $K = 4$.



(a) $k = K, t = 0.2$



(b) $k = K, t = 1.0$



(c) $k = K, t = 2.0$

Figure 15: The partition hyperplane density (left), the collocation points (middle) and the shape parameters (right) for (30) with $K = 4$ and $J_n = 4000$ at the final ($k = K$) iteration and $t = 0.2, 1.0, 2.0$

The Dirichlet boundary condition $g(x, y) = 0$ on $\partial\Omega$ and the source term $f(x, y) = 1$ on Ω . We set $b = (1, 0)^T$, $\varepsilon = 4.8 \times 10^{-4}$, $m = 2.7 \times 10^5$, $M_p = N_x \times N_y = 9 \times 1$, $\gamma_n = 3.4$, $J_n = 4000$, and the other parameters are the same as those shown in Table 1. The numerical estimation of $\phi(x, y)$ is performed using Algorithm 1. For $J_n = 4000$, Figure 16 displays the approximate solutions $\tilde{\phi}_k$ at the initial ($k = 0$) and final ($k = K = 4$) iterations. The partition hyperplane density, the collocation points and the shape parameters for $J_n = 4000$ at $k = 0$ and $k = K = 4$ iterations are shown in Figure 17.

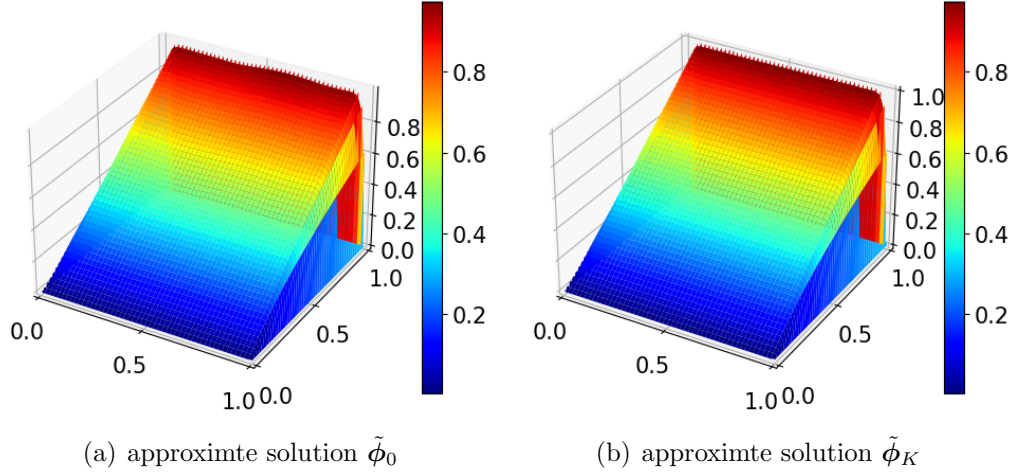
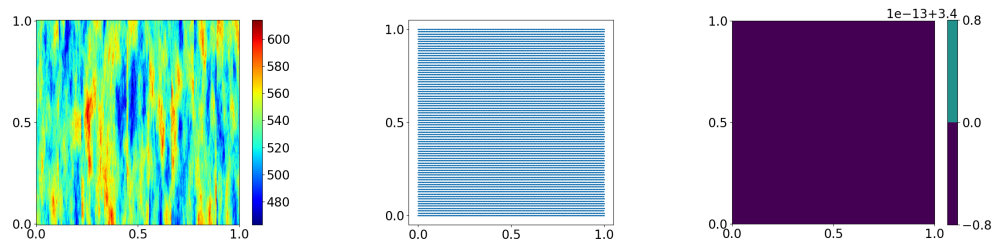


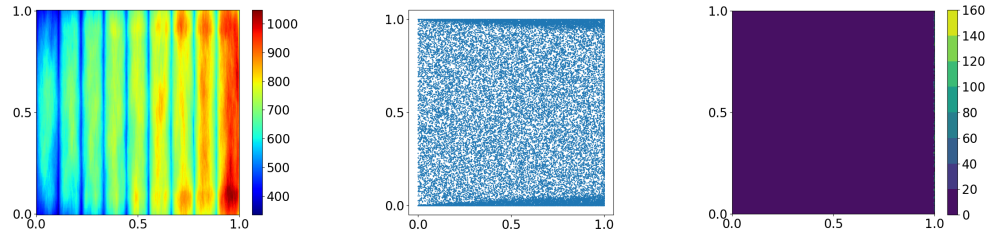
Figure 16: The approximate solutions $\tilde{\phi}_k$ at $k = 0, K$ iterations with $J_n = 4000$ and $K = 4$.

5. Conclusions and remarks

In this work, we propose the adaptive feature capture method (AFCM) based on RFM, a novel approach specifically developed to handle PDEs with low regularity solutions while maintaining high numerical accuracy without requiring additional computational resources and the prior information of the exact solutions. Building on TransNet’s initialization framework, the AFCM employs the gradient norm of the approximate solutions of RFM as an indicator. This mechanism drives the partition hyperplanes of feature functions and collocation points to concentrate in regions characterized by larger solution gradients. Within these regions, the method further enhances



(a) partition hyperplane density ($k = 0$) (b) collocation points ($k = 0$) (c) shape parameter ($k = 0$)



(d) partition hyperplane density ($k = K$) (e) collocation points ($k = K$) (f) shape parameter ($k = K$)

Figure 17: The partition hyperplane density, the collocation points and the shape parameters with $J_n = 4000$ at $k = 0$ and $k = K = 4$ iterations.

the steepness of feature functions' pre-activation values along the normal directions of the partition hyperplanes. Consequently, the AFCM achieves enhanced local expressive power in high-gradient regions, thereby yielding more accurate approximations. The AFCM repeats this adaptation process until no further improvement in the approximate solutions can be made. The proposed method delivers high accuracy in both space and time. As a mesh-free algorithm, it is inherently adaptable to complex geometric configurations and demonstrates efficacy in solving low regularity PDEs. We show a series of numerical experiments to validate our method. Results consistently confirm the stability and accuracy of the AFCM. Future work will explore extensions of this methodology to broader classes of PDEs and applications.

Acknowledgements

This research is partially supported by the National Key R & D Program of China (No.2022YFE03040002) and the National Natural Science Foundation of China (No.12371434).

References

- [1] L. Debnath, L. Debnath, Nonlinear partial differential equations for scientists and engineers, Vol. 2, Springer, 2005.
- [2] Y. Achdou, F. J. Buera, J.-M. Lasry, P.-L. Lions, B. Moll, Partial differential equation models in macroeconomics, Philosophical Transactions of the Royal Society A: Mathematical, Physical and Engineering Sciences 372 (2028) (2014) 20130397.
- [3] A. W. Leung, Systems of nonlinear partial differential equations: applications to biology and engineering, Vol. 49, Springer Science & Business Media, 2013.
- [4] R. J. LeVeque, Finite difference methods for ordinary and partial differential equations: steady-state and time-dependent problems, SIAM, 2007.
- [5] F. Moukalled, L. Mangani, M. Darwish, F. Moukalled, L. Mangani, M. Darwish, The Finite Volume Method, Springer, 2016.

- [6] V. Thomée, Galerkin Finite Element Methods for Parabolic Problems, Vol. 25, Springer Science & Business Media, 2007.
- [7] O. C. Zienkiewicz, R. L. Taylor, J. Zhu, The Finite Element Method: Its Basis and Fundamentals, Elsevier, 2005.
- [8] S. Rajendran, A technique to develop mesh-distortion immune finite elements, Computer Methods in Applied Mechanics and Engineering 199 (17-20) (2010) 1044–1063.
- [9] J. Blazek, Computational fluid dynamics: principles and applications, Butterworth-Heinemann, 2015.
- [10] I. Goodfellow, Y. Bengio, A. Courville, Deep learning, MIT press, 2016.
- [11] G. Cybenko, Approximation by superpositions of a sigmoidal function, Mathematics of control, signals and systems 2 (4) (1989) 303–314.
- [12] W. E, J. Han, A. Jentzen, Deep Learning-Based Numerical Methods for High-Dimensional Parabolic Partial Differential Equations and Backward Stochastic Differential Equations, Communications in Mathematics and Statistics 5 (5) (2017) 349–380.
- [13] J. Han, A. Jentzen, W. E, Solving high-dimensional partial differential equations using deep learning, Proceedings of the National Academy of Sciences 115 (34) (2018) 8505–8510.
- [14] W. E, B. Yu, The Deep Ritz Method: A Deep Learning-Based Numerical Algorithm for Solving Variational Problems, Communications in Mathematics and Statistics 6 (2018) 1–12.
- [15] J. Sirignano, K. Spiliopoulos, DGM: A deep learning algorithm for solving partial differential equations, Journal of computational physics 375 (2018) 1339–1364.
- [16] Y. Zang, G. Bao, X. Ye, H. Zhou, Weak adversarial networks for high-dimensional partial differential equations, Journal of Computational Physics 411 (2020) 109409.
- [17] M. Raissi, P. Perdikaris, G. E. Karniadakis, Physics-informed neural networks: A deep learning framework for solving forward and inverse

- problems involving nonlinear partial differential equations, *Journal of Computational physics* 378 (2019) 686–707.
- [18] W. E, J. Han, A. Jentzen, Algorithms for solving high dimensional PDEs: from nonlinear Monte Carlo to machine learning, *Nonlinearity* 35 (1) (2021) 278.
 - [19] Z. Lin, Y. Wang, H. Xie, Adaptive neural network subspace method for solving partial differential equations with high accuracy, *arXiv preprint arXiv:2412.02586* (2024).
 - [20] W. Zhang, W. Suo, J. Song, W. Cao, Physics Informed Neural Networks (pinns) as intelligent computing technique for solving partial differential equations: Limitation and future prospects, *arXiv preprint arXiv:2411.18240* (2024).
 - [21] G.-B. Huang, Q.-Y. Zhu, C.-K. Siew, Extreme learning machine: Theory and applications, *Neurocomputing* 70 (1-3) (2006) 489–501.
 - [22] R. M. Neal, *Bayesian learning for neural networks*, Vol. 118, Springer Science & Business Media, 2012.
 - [23] A. Rahimi, B. Recht, Random features for large-scale kernel machines, in: *Proceedings of the 21st International Conference on Neural Information Processing Systems*, Curran Associates Inc., 2007, p. 1177–1184.
 - [24] G. Huang, G.-B. Huang, S. Song, K. You, Trends in extreme learning machines: A review, *Neural Networks* 61 (2015) 32–48.
 - [25] J. Chen, X. Chi, Z. Yang, et al., Bridging Traditional and Machine Learning-Based Algorithms for Solving PDEs: The Random Feature Method, *J Mach Learn* 1 (2022) 268–98.
 - [26] J. Chen, Y. Luo, et al., The Random Feature Method for Time-dependent Problems, *arXiv preprint arXiv:2304.06913* (2023).
 - [27] G.-B. Huang, L. Chen, C.-K. Siew, Universal Approximation using Incremental Constructive Feedforward Networks with Random Hidden Nodes, *IEEE transactions on neural networks* 17 (4) (2006) 879–892.

- [28] V. Dwivedi, B. Srinivasan, Physics Informed Extreme Learning Machine (PIELM)—A rapid method for the numerical solution of partial differential equations, *Neurocomputing* 391 (2020) 96–118.
- [29] F. Calabrò, G. Fabiani, C. Siettos, Extreme learning machine collocation for the numerical solution of elliptic PDEs with sharp gradients, *Computer Methods in Applied Mechanics and Engineering* 387 (2021) 114188.
- [30] S. Dong, Z. Li, Local extreme learning machines and domain decomposition for solving linear and nonlinear partial differential equations, *Computer Methods in Applied Mechanics and Engineering* 387 (2021) 114129.
- [31] G. Fabiani, F. Calabrò, L. Russo, C. Siettos, Numerical solution and bifurcation analysis of nonlinear partial differential equations with extreme learning machines, *Journal of Scientific Computing* 89 (2) (2021) 44.
- [32] Y. Yang, M. Hou, J. Luo, A novel improved extreme learning machine algorithm in solving ordinary differential equations by Legendre neural network methods, *Advances in Difference Equations* 2018 (1) (2018) 469.
- [33] Y. Wang, S. Dong, An extreme learning machine-based method for computational pdes in higher dimensions, *Computer Methods in Applied Mechanics and Engineering* 418 (2024) 116578.
- [34] H. Dang, F. Wang, S. Jiang, Adaptive growing randomized neural networks for solving partial differential equations, *arXiv preprint arXiv:2408.17225* (2024).
- [35] J. Sun, S. Dong, F. Wang, Local randomized neural networks with discontinuous Galerkin methods for partial differential equations, *Journal of Computational and Applied Mathematics* 445 (2024) 115830.
- [36] J. Huang, H. Wu, T. Zhou, Adaptive neural network basis methods for partial differential equations with low-regular solutions, *arXiv preprint arXiv:2411.01998* (2024).

- [37] W. Ren, X. Wang, An iterative grid redistribution method for singular problems in multiple dimensions, *Journal of Computational Physics* 159 (2000) 246–273.
- [38] W. Huang, R. D. Russell, *Adaptive Moving Mesh Method*, Springer, 2010.
- [39] J. I. Ramos, Picard’s iterative method for nonlinear advection–reaction–diffusion equations, *Applied Mathematics and Computation* 215 (4) (2009) 1526–1536.
- [40] Z. Zhang, F. Bao, L. Ju, G. Zhang, Transferable Neural Networks for Partial Differential Equations, *Journal of Scientific Computing* 99 (1) (2024) 2.